Regional Tropical Precipitation Change Mechanisms in ECHAM4/OPYC3 under Global Warming*

CHIA CHOU

Research Center for Environmental Changes, Academia Sinica, Taipei, Taiwan

J. DAVID NEELIN

Department of Atmospheric Sciences, and Institute of Geophysics and Planetary Physics, University of California, Los Angeles, Los Angeles, California

JIEN-YI TU

Research Center for Environmental Changes, Academia Sinica, Taipei, Taiwan

CHENG-TA CHEN

Department of Earth Sciences, National Taiwan Normal University, Taipei, Taiwan

(Manuscript received 25 July 2005, in final form 20 December 2005)

ABSTRACT

Mechanisms of global warming impacts on regional tropical precipitation are examined in a coupled atmosphere–ocean general circulation model (ECHAM4/OPYC3). The pattern of the regional tropical precipitation changes, once established, tends to persist, growing in magnitude as greenhouse gases increase. The sulfate aerosol induces regional tropical precipitation anomalies similar to the greenhouse gases but with opposite sign, thus reducing the early signal. Evidence for two main mechanisms, the upped-ante and the anomalous gross moist stability (M') mechanisms (previously proposed in an intermediate complexity model), is found in this more comprehensive coupled general circulation model. Preferential moisture increase occurs in convection zones. The upped-ante mechanism signature of dry advection from nonconvective regions is found in tropical drought regions on the margins of convection zones. Here advection in both the atmospheric boundary layer and lower free troposphere are found to be important, with an additional contribution from horizontal temperature transport in some locations. The signature of the M' mechanism—moisture convergence due to increased moisture in regions of large mean vertical motion—enhances precipitation within strong convective regions. Ocean dynamical feedbacks can be assessed by net surface flux, the main example being the El Niño–like shift of the equatorial Pacific convection zone. Cloud–radiative feedbacks are found to oppose precipitation anomalies over ocean regions.

1. Introduction

Anthropogenic forcings, such as greenhouse gases and aerosols, are starting to change the global climate. The recent and projected future warming tendency has been extensively studied with coupled atmosphere–ocean general circulation model (Manabe et al. 1991; Hansen et al. 1995; and recent studies, e.g., Watterson and Dix 1999; Boer et al. 2000; Dai et al. 2001b; Delworth and Knutson 2000; Held and Soden 2000; Meehl et al. 2000; Mitchell et al. 2000; Washington et al. 2000; Houghton et al. 2001; Yonetani and Gordon 2001; Lucarini and Russell 2002; Meehl et al. 2005). Projected tropical precipitation changes are large in many climate models (e.g., Roeckner et al. 1999; Boer et al. 2000; Meehl et al. 2000; Dai et al. 2001a; Williams et al. 2001; Allen and Ingram 2002; Douville et al. 2002; Meehl et al. 2003). However, little agreement on regional tropi-

* Institute of Geophysics and Planetary Physics, University of California, Los Angeles, Contribution Number 6243.

Corresponding author address: Chia Chou, Research Center for Environmental Changes, Academia Sinica, P.O. Box 1-48, Taipei 11529, Taiwan.
E-mail: chiachou@rcec.sinica.edu.tw

cal precipitation changes is found among models since these involve complicated processes in interaction of large-scale dynamics and tropical convection (e.g., Houghton et al. 2001; Neelin et al. 2003, hereafter NCS03). Unlike the temperature change, which is warming almost everywhere, the precipitation change has a strong spatial variation with positive and negative anomalies on a regional scale.

Chou and Neelin (2004, hereafter CN04) examined mechanisms of global warming impacts on regional tropical precipitation by using an atmospheric model of intermediate complexity [the quasi-equilibrium tropical circulation model (QTCM)] coupled with a mixed layer ocean (Neelin and Zeng 2000; Zeng et al. 2000). In their study, two dominant mechanisms are responsible for regional tropical precipitation anomalies: the upped-ante mechanism and the anomalous gross moist stability (M') mechanism. Under convective quasi-equilibrium (QE), the low-level moisture over convective regions is enhanced in response to the warming induced by the greenhouse effect. The effect linking low-level moisture with tropospheric temperature is termed "QE mediation" (Neelin and Su 2005). This QE mediation does not influence low-level moisture over nonconvective regions, which is affected by different processes, such as a balance between horizontal moisture advection and evaporation, so the increase of low-level moisture is less over nonconvective regions than over convective regions. This creates a horizontal gradient of low-level moisture anomalies, which is fundamental for the upped-ante and M' mechanisms. In the upped-ante mechanism, the precipitation over margins of convective regions is reduced by import of dry air where there is mean inflow from nonconvective regions to convective regions. This occurs via the term $-\mathbf{v} \cdot \nabla q$. In the M' mechanism, low-level moisture is increased over convective regions due to QE mediation. This decreases the effective static stability M. As a result, convergence and convection are enhanced in regions that had strong convergence and precipitation in the climatology. This mechanism is thus also referred to as the "rich-get-richer" mechanism.

To what extent can the mechanisms discussed in CN04 be applied to a more comprehensive climate model, such as a coupled atmosphere–ocean general circulation model (AOGCM)? To answer this question is our primary goal and the ECHAM4/OPYC3 AOGCM simulations (Roeckner et al. 1999) are analyzed in this study. The model and experiment design are described in section 2. Since simulations with and without sulfate aerosol are available, we also briefly examine the role of sulfate aerosol on regional tropical precipitation in section 3. Comparisons of the AOGCM with a coupled atmospheric GCM and mixed layer ocean model discussed in section 4 isolate the role of ocean dynamical feedback. To examine those mechanisms of global warming impacts on regional tropical precipitation that are found in CN04, moisture and moist static energy (MSE) budgets are discussed and the budgets of the AOGCM simulations are diagnosed in section 5.

2. Model and experiments

The AOGCM used in this study is the ECHAM4/OPYC3 model (Roeckner et al. 1999). The atmospheric component is the fourth-generation Max Planck Institute for Meteorology model (ECHAM4; Roeckner et al. 1996). The ECHAM4 model uses a 19-level sigma-pressure coordinate system up to 10 hPa and prognostic equations represented by spherical harmonics with triangular truncation at wavenumber 42 (T42). In the model, the tropospheric sulfate cycle is simulated and the associated sulfate aerosol is calculated to estimate aerosol effects. The oceanic component of the AOGCM is an extended version of the OPYC model, which contains the interior ocean, the surface mixed layer, and sea ice. A detailed description can be found in Oberhuber (1993). To examine ocean dynamical feedbacks, the ECHAM4 model with T30 resolution is also coupled to a 50-m slab mixed layer ocean model with prescribed seasonal ocean heat transport and the results are compared to the AOGCM simulations.

Based on the Intergovernmental Panel on Climate Change (IPCC) scenario IS92a (CO_2 concentration increasing at 1% per year after 1990; Houghton et al. 1992), several global warming experiments with the ECHAM4/OPYC3 model have been performed at the Max Planck Institute for Meteorology (MPI). All runs are transient experiments in which greenhouse gases (GHGs) and aerosol are time dependent and are as described in Roeckner et al. (1999). The first global warming experiment is only forced by GHGs that are updated with observed values before 1990 and projected values after 1990. The second experiment [GHG plus sulfate aerosol direct and indirect effect and tropospheric ozone (GSDIO)] includes the tropospheric sulfate cycle in addition to the same greenhouse gases in the GHG experiment. Aerosol direct and indirect effects are included, the latter with a parameterization of the sulfate aerosol effect on cloud albedo. The tropospheric ozone distribution also changes with prescribed anthropogenic precursor emissions. The GHG experiment ends in 2100, while GSDIO is only until 2050. Note that the GSDIO experiment only includes sulfate aerosols. Other aerosol components, such as mineral dust and black carbon, are not included.

Averages from 1961 to 1990 are used to represent current climate. The CO_2 concentration is doubled around 2070–99. Two experiments with the ECHAM4 model coupled to the mixed layer ocean model (ML) done by the MPI are also used. The first is a control experiment, which is a 1000-yr run; data between years 800 and 899 are used. The other experiment is an equilibrium doubled CO_2 run for 50 yr. Data between years 30 and 50 are used since data before year 30 are spinup. Output from these simulations is used to examine mechanisms for regional tropical precipitation change under global warming.

3. Long-term regional precipitation: GHG versus aerosol contribution

Figure 1 shows impacts of GHGs on precipitation and tropospheric temperature in the GHG experiment. The precipitation and temperature perturbations are the differences between 2021–50 and 1961–90. The largest magnitude of precipitation changes induced by GHG is concentrated in the Tropics and has both positive and negative regions. The positive precipitation anomalies over the Indian Ocean in June–August (JJA) and December–February (DJF) and over South America in DJF are mostly in convective regions. However, the positive anomalies over the equatorial Pacific Ocean are shifted slightly eastward, particularly in the winter season. The positive JJA precipitation anomalies over Africa indicate a northward shift of the convective region. Other negative precipitation anomalies are found over the southern and northern sides of intertropical convergence zone (ITCZ), such as those over the Indian and Pacific Oceans. Some negative precipitation anomalies are found over the eastern side of convective regions, such as the South Pacific convergence zone (SPCZ) and the South American convective region. Most of these regions with negative precipitation anomalies are over the margins of deep convection regions where mean flow imports air from nonconvective regions. For instance, the precipitation anomalies in two target regions (the boxes in Fig. 1b) are roughly about -0.76 and -0.59 mm day^{-1} averaged over the margins of the Indian Ocean and South American convective regions, respectively. Here the region with climatological precipitation between 3 and 6 mm day^{-1} has been used as a simple definition of the convective margin. The changes of precipitation described above are qualitatively consistent with the ensemble mean change of precipitation (e.g., Allen and Ingram 2002; Houghton et al. 2001) based on multiple AOGCM simulations.

The tropospheric temperature anomalies are positive everywhere (Figs. 1c,d). In the boreal summer, the tropospheric temperature anomalies have a maximum warming at high latitudes of the Northern Hemisphere and a minimum warming at high latitudes of the Southern Hemisphere. In the boreal winter, the warm temperature anomalies at high latitudes of the Northern Hemisphere are weakened, so the maximum warm tropospheric temperature anomalies are found over the Tropics. This indicates that the tropospheric temperature anomalies at high latitudes of the Northern Hemi-

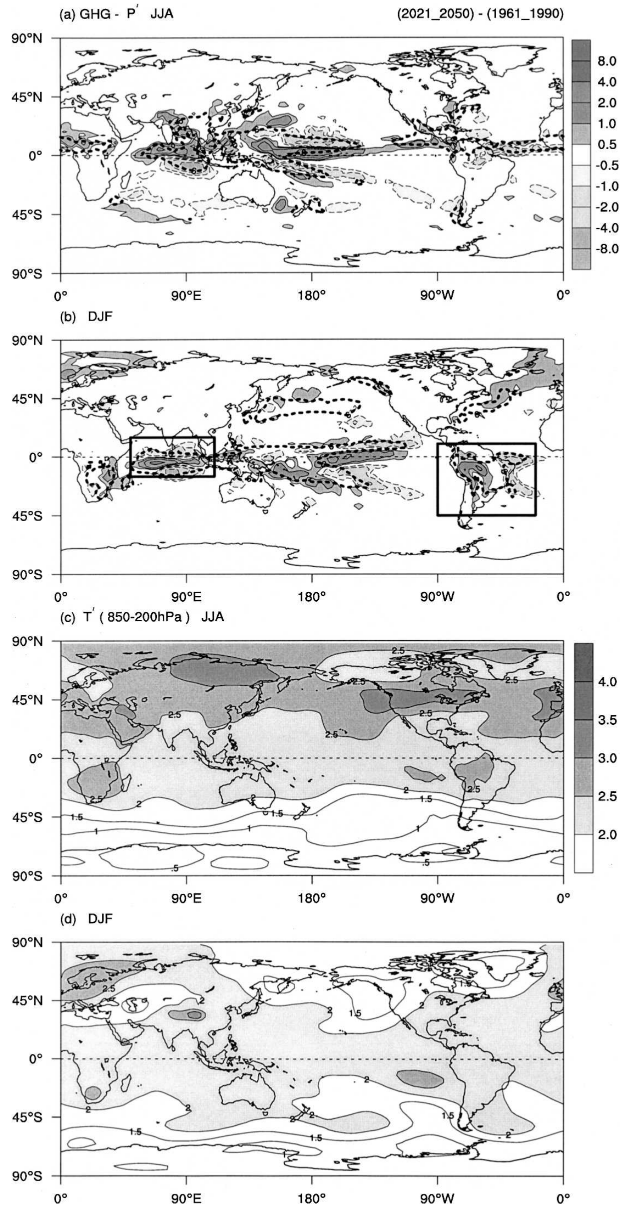

Fig. 1. Differences for the 2021–50 averages minus the 1961–90 climatology for the GHG experiment. Precipitation (mm day^{-1}) in (a) JJA and (b) DJF and tropospheric temperature (°C; 850–200 hPa) in (c) JJA and (d) DJF. The thick dashed line in (a) and (b) is the 6 mm day^{-1} contour of the precipitation climatology in 1961–90. The two boxes are the target regions (see text).

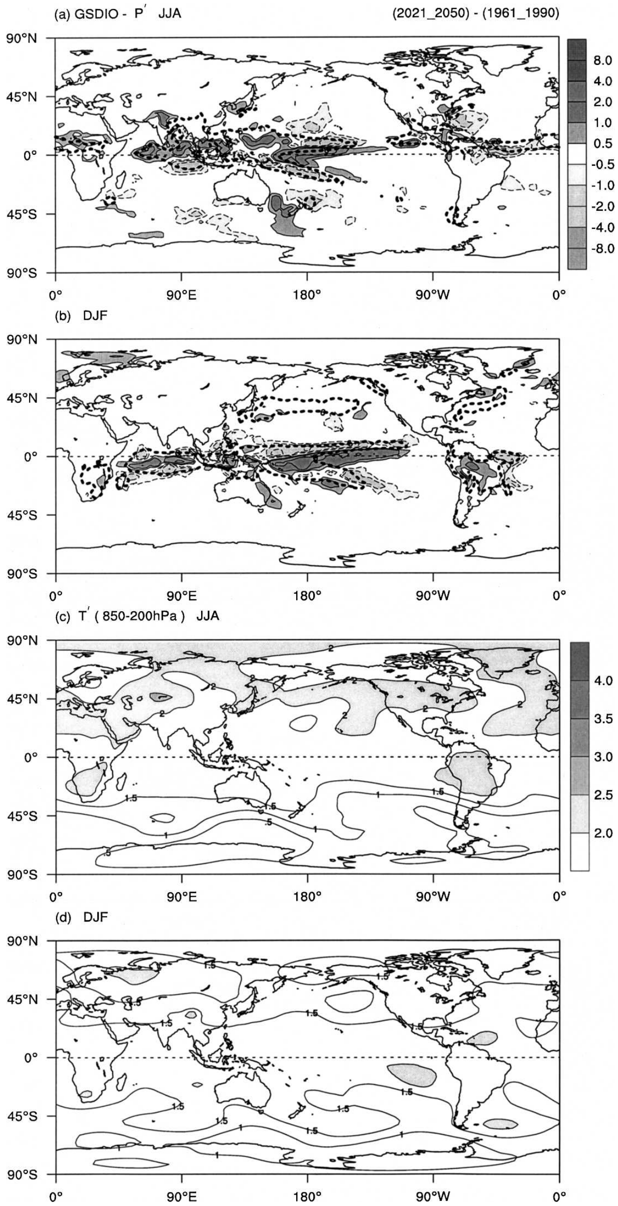

FIG. 2. Same as in Fig. 1 except for the GSDIO experiment.

sphere have a strong annual cycle, while the annual cycle of tropospheric temperature anomalies over the rest of the world is much weaker. This pattern of the tropospheric temperature anomalies in the boreal winter is similar to the pattern of the tropospheric temperature anomalies in El Niño (Wallace et al. 1998; Su et al. 2003) in which the warmer sea surface temperature (SST) in the eastern Pacific warms the tropical troposphere via tropical convection and wave dynamics.

Figure 2 shows the results in the GSDIO experiment in which the direct and indirect effects of sulfate aerosol are included. The overall patterns of the precipitation anomalies are similar to those in Fig. 1. However, the amplitude of the precipitation anomalies is weaker for most regions, except for the central Pacific in the boreal winter. Interdecadal variance (not shown) is higher in the Pacific, and so might affect this. The sulfate aerosol has strong spatial variations (Fig. 4 of Roeckner et al. 1999), but the similar spatial distribution of the precipitation anomalies in Figs. 1 and 2 implies that the aerosol local effect is small compared to the greenhouse effect even over those areas where sulfate aerosol concentration is high. The warm tropospheric temperature anomalies in Fig. 2 are also weaker than those in the GHG experiment (Figs. 1c,d). The sulfate aerosol reflects solar radiation and cools the troposphere, and then the cold temperature anomalies are spread globally by wave dynamics. Thus, the warm tropospheric temperature anomalies induced by greenhouse gases are weakened with little change in its global spatial pattern. The weakened temperature anomalies induce aerosol remote effects, such as the anomalous gross moist stability (M') and upped-ante mechanisms (Chou et al. 2005), which have similar impacts on regional precipitation to the global warming case, but with the opposite sign. For a tropical average, the aerosol effects reduce the tropospheric temperature anomalies by about 22% in the GHG experiment while the reduction of the root-mean-square of the precipitation anomalies is around 12%. The difference (not shown) tends to look like the pattern in Fig. 1 with the opposite sign (i.e., a reduction in the GHG precipitation). The point-by-point correlation of the (GSDIO − GHG) pattern to the GHG pattern for all 12 months is -0.61 within 20°S–20°N for those differences greater than 0.5 mm day^{-1}. The regression coefficient is -0.57 (i.e., aerosol effects tend to cancel a substantial part of the GHG induced precipitation pattern). The part of the (GSDIO − GHG) difference that does not correlate with the GHG pattern contributes little, so the root-mean-square reduction is not as large.

While in the long term the GHG effects tend to dominate, it is of interest to see what signal might exist in the period of present observations, including the contribution of aerosols. The results of the GSDIO experiments in the earlier period (1981–2000) is shown in Fig. 3 when the greenhouse effect is relatively weak and the aerosol local effect may be relatively important. The 20-yr averaging and the relatively weaker signal imply caveats with respect to decadal variability. A comparison of Figs. 3a,b to Figs. 2a,b in terms of pattern gives some sense to what signal might be detectable despite decadal variability. There is some resemblance between the patterns although there are also many regions

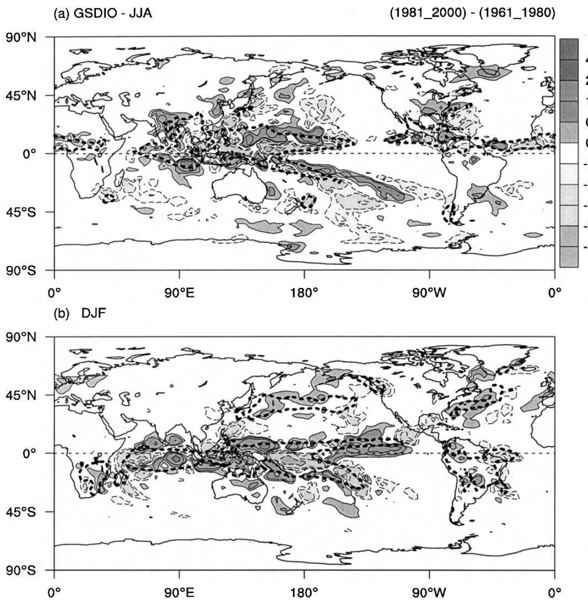

FIG. 3. Precipitation differences (mm day^{-1}) between the 1981–2000 and 1961–80 averages for the GSDIO experiment in (a) JJA and (b) DJF.

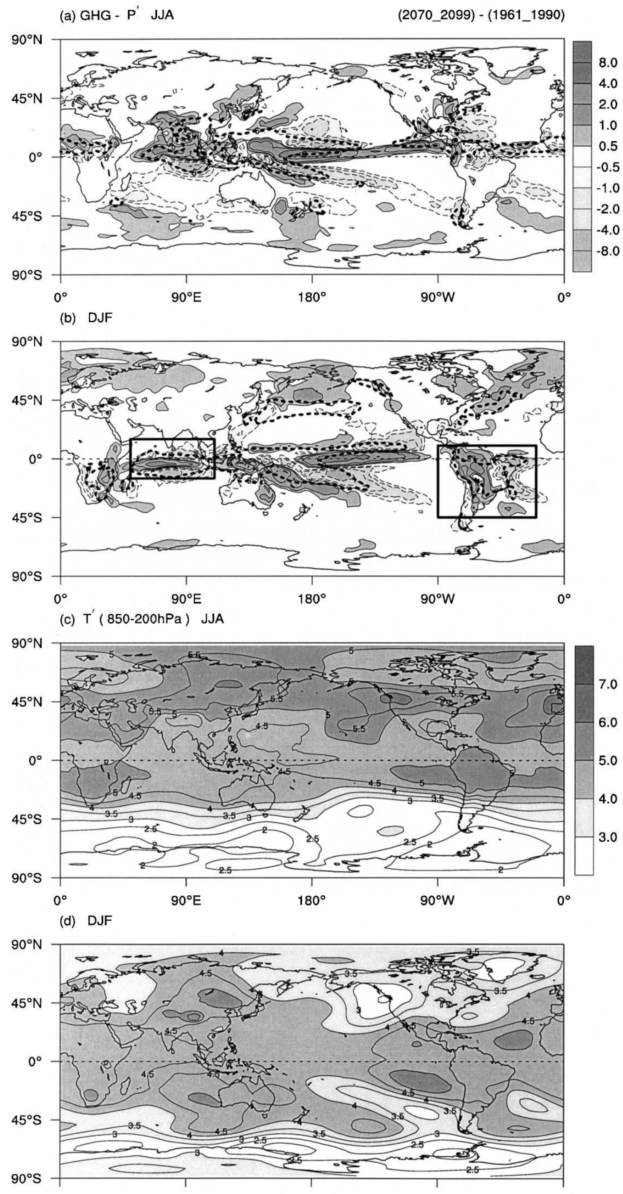

FIG. 4. Same as in Fig. 1 except for differences between 2070–99 and 1961–90.

where substantial differences occur due to decadal variability. This suggests that it may be challenging to infer the long-term GHG effect reliably from recent observed trends, except for particular regions such as eastern South America in DJF and the Caribbean in JJA.

4. Atmospheric versus oceanic feedbacks

To understand the oceanic feedbacks, we compare experiments with the ECHAM4 atmospheric model coupled with an ML ocean, with normal and doubled carbon dioxide concentrations, respectively. This pair of experiments with no ocean feedback (Fig. 5) is compared to the GHG experiment with differences between 1961–90 and 2070–99 (Fig. 4) when carbon dioxide concentration is roughly doubled. Note that besides the difference in oceanic feedback, the ML experiments are an equilibrium simulation, but the GHG experiment is a transient simulation. For the longer GHG simulation shown in Fig. 4, the spatial distributions of the precipitation and tropospheric temperature anomalies are very similar to the anomalies in the earlier period shown in Fig. 1, but with stronger amplitude. This implies that the changes in temperature and precipitation induced by the greenhouse effect are already established in 2021–50 and the patterns tend to grow and persist over the century. Most tropical precipitation anomalies in the ML experiments (Fig. 5) are similar to those in the GHG experiment when ocean dynamical feedback is included (Fig. 4), except for the Pacific. In the Pacific, oceanic feedback tends to shift the positive precipitation anomalies eastward. Without oceanic feedback, almost all positive precipitation anomalies in the Tropics occur over convective regions, while the negative precipitation anomalies occur over margins of convective regions [e.g., South America and the Indian Ocean in DJF (the boxes in Fig. 5b)]. This distribution of the regional tropical precipitation anomalies (Fig. 5) is very similar to those found in CN04. In their study, they also used an ML ocean without considering ocean

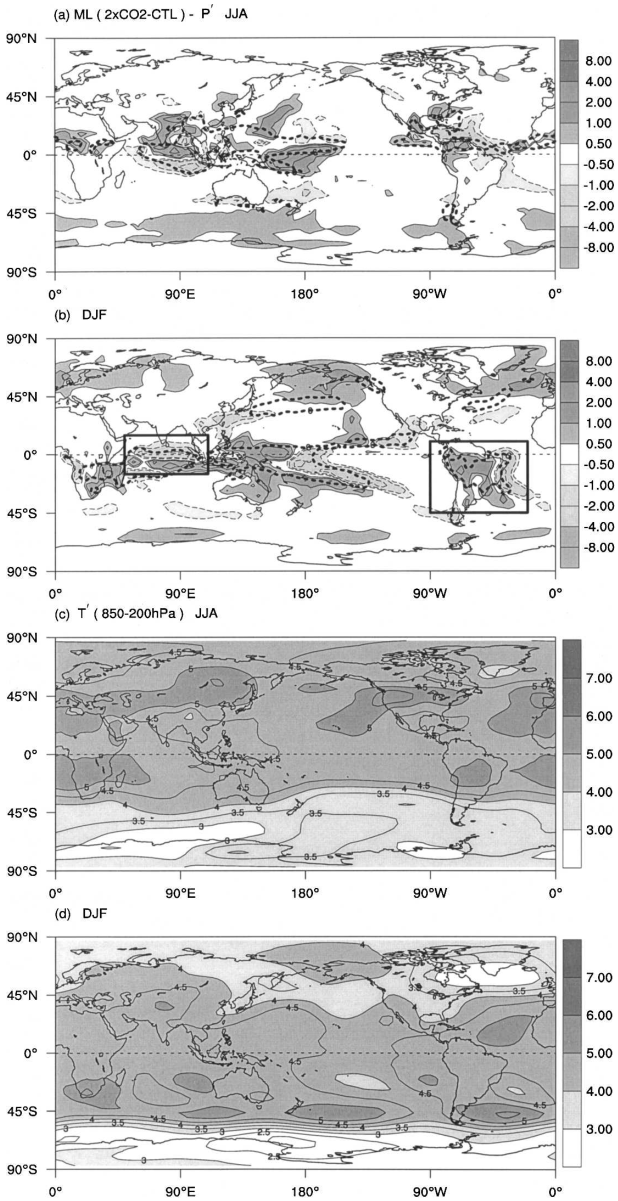

FIG. 5. Same as in Fig. 4 except for the ML experiment, which is an equilibrium doubled CO_2 simulation.

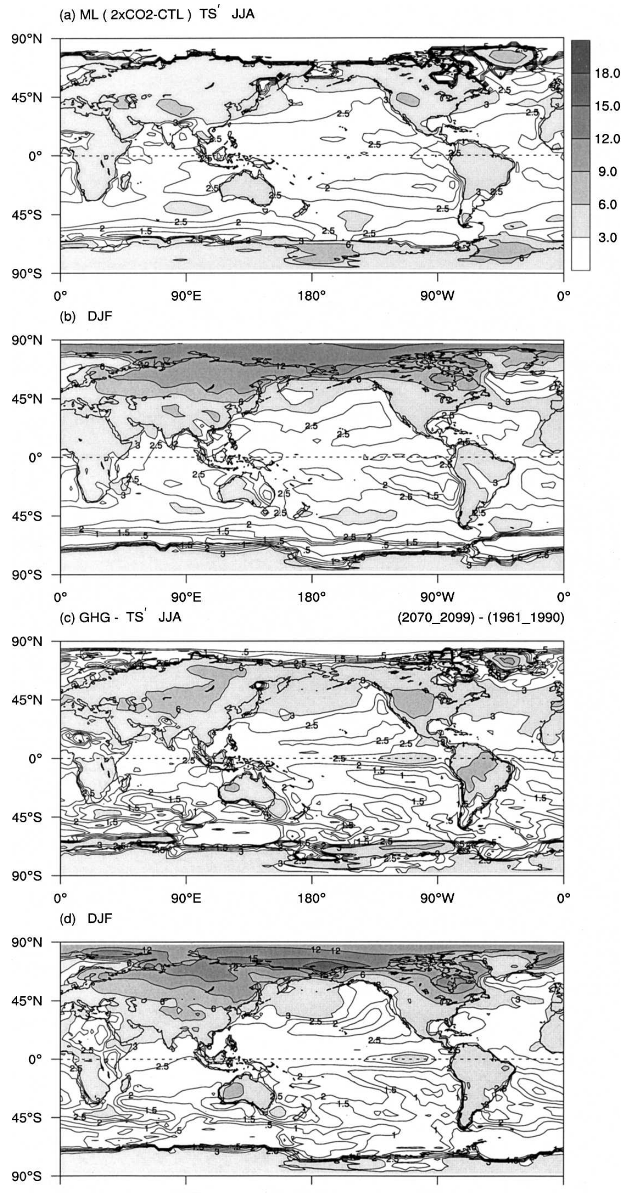

FIG. 6. Surface temperature differences (°C) for the ML experiment in (a) JJA and DJF and the GHG experiment 2070–99 minus 1961–90 averages in (c) JJA and (d) DJF.

dynamical feedback. Those areas with similar precipitation anomaly patterns in Figs. 4 and 5, such as South America and the Indian Ocean, can be good target regions to examine the mechanisms of global warming impacts on regional precipitation that are discussed in CN04. The tropospheric temperature anomalies are surprisingly similar in Figs. 4 and 5. The only visible difference is that warmer temperature anomalies are found over the high latitudes of the Southern Hemisphere in JJA when there is no oceanic feedback (Fig. 5c).

To examine ocean dynamical feedback, we first compare surface temperature anomalies between the GHG and ML experiments (Fig. 6). For most areas, the results in the two experiments are quite similar. Surface temperature anomalies are warmer over land than over ocean. The high latitudes of the Northern Hemisphere in DJF have maximum surface temperature anomalies due to a reduction of snow and sea ice cover in the Northern Hemisphere (Houghton et al. 2001). This seasonal variation of the surface temperature anomalies over the Northern Hemisphere is different from the mid- and upper-tropospheric temperature anomalies

(850–200 hPa) shown in Figs. 4c,d. The tropospheric temperature anomalies have a maximum at high latitudes of the Northern Hemisphere in JJA. In the Pacific, the SST anomalies between these two experiments are very different. With ocean dynamical feedback, a clear El Niño–like SST anomaly pattern is found (Figs. 6c,d), but this SST anomaly pattern is not found in the ML experiments (Figs. 6a,b). It indicates that the ocean dynamical feedback in the ECHAM4 AOGCM global warming simulations exhibits similar impacts to those found in El Niño events, which has been discussed in various studies (e.g., Tett 1995; Meehl and Washington 1996; Knutson and Manabe 1998; Roeckner et al. 1999; Jin et al. 2001; Watterson 2003). That is why the positive precipitation anomalies over the Pacific shift eastward in Figs. 4a,b. An El Niño–like horseshoe pattern of negative precipitation anomalies is also found over the eastern Pacific. Note that this El Niño–like response in SST anomalies is not found in every climate model simulation. For instance, Noda et al. (1999) shows smaller warming anomalies over the eastern Pacific.

To further study the ocean dynamical feedback under global warming, net surface heat flux anomalies F_s' are examined and the results are shown in Fig. 7. With ocean dynamical feedback, the variations of the net surface heat flux anomalies are much stronger. The net surface heat flux is balanced by ocean heat storage and transport. An overall negative net surface heat flux anomaly averaged over the globe indicates that the ocean acts as a heat sink. The ocean is warmed relatively slower than the atmosphere and land because of its heat capacity, so the ocean tends to delay the global warming induced by the greenhouse effect (e.g., Manabe et al. 1991). This lag response induced by ocean heat capacity can affect tropical precipitation via tropospheric temperature changes (CN04). Another different feature between the GHG and ML experiments are positive heat flux anomalies in the equatorial central and eastern Pacific. This is consistent with the El Niño–like warm SST anomaly pattern found in Fig. 6. The regional F_s' is associated with ocean heat transport and it can reach as large as 40 W m^{-2} (e.g., in the Pacific cold tongue). Besides the Pacific cold tongue, the western Indian Ocean in JJA also exhibits positive surface heat flux anomalies due to ocean dynamical feedback. Both the Pacific cold tongue and the western Indian Ocean have strong upwelling. Large regional F_s' does not necessarily induce stronger precipitation anomalies, such as at high latitudes. It is only the regions that have large F_s' and occur in or near-tropical convection zones that ocean dynamical feedback is important for precipitation changes. Otherwise, the atmospheric circulation is the dominant factor for inducing the precipitation anomalies.

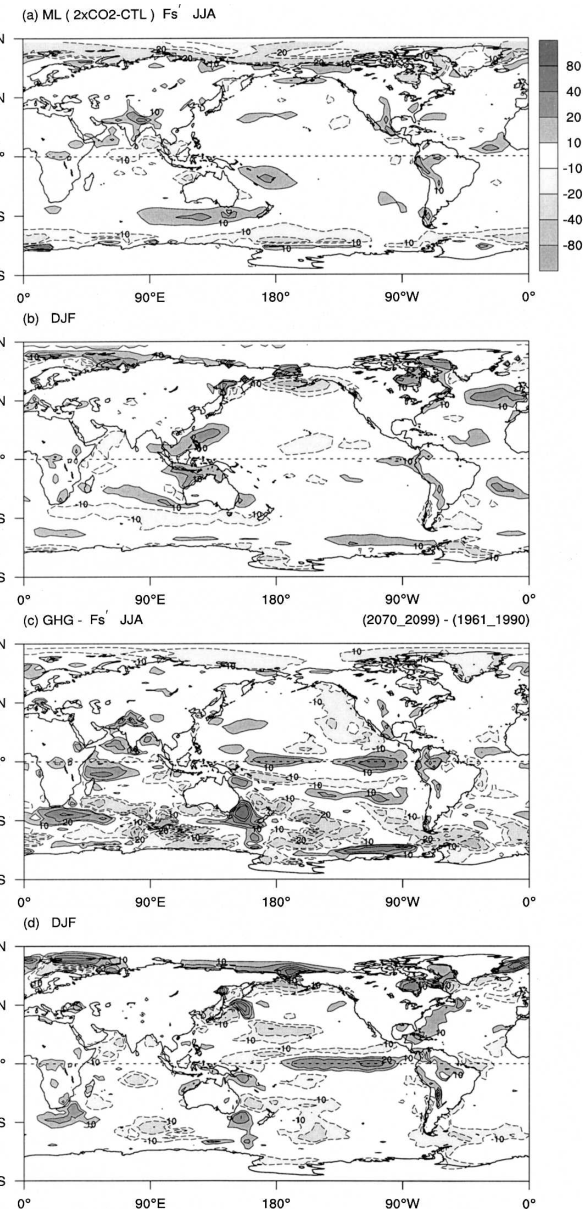

Fig. 7. Same as in Fig. 6 except for surface heat flux (W m^{-2}).

5. Diagnosis of regional precipitation mechanisms

a. Moisture and moist static energy (MSE) budget

The anomalous regional precipitation under global warming can be obtained from the vertically integrated moisture equation in a steady state, with the vertical integral $\langle\rangle$ over the troposphere defined as

$$\langle X \rangle = \frac{1}{g} \int_{p_s}^{p_s - p_T} X \, dp, \qquad (1)$$

where g is gravity, p_T is the depth of the troposphere, and p_s is surface pressure. The moisture equation for departures from current climate is then

$$P' \approx -\langle \omega' \partial_p \overline{q} \rangle - \langle \overline{\omega} \partial_p q' \rangle - \langle \mathbf{v}' \cdot \nabla \overline{q} \rangle - \langle \overline{\mathbf{v}} \cdot \nabla q' \rangle + E', \tag{2}$$

where P is precipitation, E is evaporation, $\mathbf{v}$ is horizontal velocity, and ω is pressure velocity. The specific humidity q is in energy units, absorbing the latent heat per unit mass, L. $\overline{(\,)}$ denotes climatology in the current climate (the period of 1961–90) and $(\,)'$ is a departure from the current climate.

The term $-\langle \omega' \partial_p \overline{q} \rangle$ is an atmospheric dynamical feedback associated with anomalous vertical motion (ω'). To understand mechanisms that induce this anomalous vertical motion, the MSE budget is analyzed. The vertically integrated MSE equation in a steady state can be written as

$$\langle \omega' \partial_p \overline{h} \rangle \approx -\langle \overline{\omega} \partial_p s' \rangle - \langle \overline{\omega} \partial_p q' \rangle - \langle \mathbf{v}' \cdot \nabla(\overline{q} + \overline{T}) \rangle - \langle \overline{\mathbf{v}} \cdot \nabla(q' + T') \rangle + F_s' + F_t', \tag{3}$$

where $h = s + q$ is moist static energy and $s = T + \phi$ is dry static energy, with ϕ being the geopotential.

The atmospheric temperature T is in energy units, absorbing the heat capacity at constant pressure, C_p. The net energy input into the atmospheric column F^{net} is given by

$$F^{\text{net}} = F_t + F_s, \tag{4}$$

where the net heat flux at the top of the atmosphere (TOA) can be obtained by

$$F_t = S_t^{\downarrow} - S_t^{\uparrow} - R_t^{\uparrow}, \tag{5}$$

and the net heat flux at the surface is

$$F_s = S_s^{\uparrow} - S_s^{\downarrow} - R_s^{\downarrow} + R_s^{\uparrow} + E + H. \tag{6}$$

Subscripts s and t on the solar ($S^{\downarrow}$ and $S^{\uparrow}$) and longwave ($R^{\uparrow}$ and $R^{\downarrow}$) radiative terms denote surface and model top, and $R_t^{\downarrow} \approx 0$ has been used. Here H is the sensible heat flux. Positive values of F_t and F_s indicate heat fluxes into the atmospheric column.

The nonlinear effects of transients and changes between current and warmer climate, $-\langle \omega' \partial_p h' \rangle$, are neglected. Since only monthly means are used in this study, we cannot calculate the contribution of transients in the ECHAM4/OPYC3 simulations. Transients can be important in climatology; but for anomalies, their role is believed to be secondary in models where the precipitation occurs primarily through a smooth convective parameterization. This holds in QTCM simulations (CN04), although counterexamples are known (e.g., Neelin 1987). The effect of transients should be examined in other model simulations in the future. The other term, the contribution from changes in vertical velocity ω and moist static energy h between 1961–90 and 2070–99, is important only when the mean state changes. For instance, the warm SST over the equatorial eastern Pacific can shift the mean state over this region from nonconvective regions to convective regions, so the nonlinear effect of $-\langle \omega' \partial_p h' \rangle$ becomes important. For most areas of interest, however, $-\langle \omega' \partial_p h' \rangle$ is secondary.

b. Background for budget interpretation

Before diagnosing the moisture and MSE budgets in (2) and (3), we first interpret the physical meaning of each term based on the derivation used in CN04. The approximations in this presentation are used only in the interpretation, not in the GCM diagnostics.

Defining a typical vertical profile of vertical motion $\Omega(p)$ that is associated with deep convection such that $\omega \approx -\Omega(p)\nabla \cdot \mathbf{v}_1$ (where Ω is assumed to vary slowly in space) yields

$$-\langle \omega' \partial_p \overline{q} \rangle \approx \overline{M}_q \nabla \cdot \mathbf{v}_1', \tag{7}$$

where $\nabla \cdot \mathbf{v}_1$ is the divergence induced by baroclinic winds and

$$M_q = \langle \Omega \partial_p q \rangle. \tag{8}$$

Positive $\nabla \cdot \mathbf{v}_1$ indicates low-level convergence and upper-level divergence in baroclinic flow. Thus, the dynamical feedback to the anomalous precipitation in (2) is directly linked to low-level convergence with a factor $\overline{M}_q$, which is associated with vertical distribution of moisture in convective regions.

Following the similar derivation to (7), $\langle \omega' \partial_p \overline{h} \rangle \approx \overline{M} \nabla \cdot \mathbf{v}_1'$ and $\langle \omega' \partial_p \overline{s} \rangle \approx \overline{M}_s \nabla \cdot \mathbf{v}_1'$ with $M = \langle -\Omega \partial_p h \rangle$ and $M_s = \langle -\Omega \partial_p s \rangle$. Thus, $\nabla \cdot \mathbf{v}_1'$ obtained from the MSE budget equation can be used in (2) to estimate the anomalous precipitation that under the above approximations is

$$P' \approx \frac{\overline{M}_q}{\overline{M}} [-\langle \overline{\omega} \partial_p s' \rangle - \langle \mathbf{v}' \cdot \nabla \overline{T} \rangle - \langle \overline{\mathbf{v}} \cdot \nabla T' \rangle + F_s' + F_t'] + E' - \left(\frac{\overline{M}_q}{\overline{M}} + 1 \right) [\langle \overline{\omega} \partial_p q' \rangle + \langle \mathbf{v}' \cdot \nabla \overline{q} \rangle + \langle \overline{\mathbf{v}} \cdot \nabla q' \rangle]. \tag{9}$$

While we do not actually use (9) in the GCM diagnostics, it provides the conceptual background for interpreting terms like $\langle \overline{\omega} \partial_p q' \rangle$ in the GCM. In (9), the anomalous precipitation is associated with the terms found in (2) and (3), but with a factor $(\overline{M}_q / \overline{M})$. In convective regions, the gross moist stability M measures static stability of large-scale motion and the convective available potential energy (CAPE) measures static stability of convective system. The value of M is determined by the low-level moisture effect and the cloud-top effect (Yu et al. 1998). The greater low-level moisture enhances convection, and thus increases M_q and decreases M. On the other hand, the stronger convection with higher convection height enhances M. This indicates a strong cancellation of the low-level moisture effect and the cloud-top effect, so a relatively constant M is found in convective regions. More detailed discussion of M can be found in Yu et al. (1998).

The sum of $\langle\overline{\omega}\partial_p s'\rangle$ and $\langle\overline{\omega}\partial_p q'\rangle$ is associated with the M' mechanism (CN04) if T' is associated with free tropical warming and q' in the atmospheric boundary layer (ABL) is also enhanced by the warming. The enhancement of the ABL moisture modifies the static stability of convective regions and produces negative M'. The atmosphere in convective regions becomes easier to convert, so the convection and the associated precipitation are enhanced. The stronger convection can increase convection height and then produce positive M'. Thus, M' depends on convection height, which is sensitive to cumulus parameterization. Because of the dependence of M on convection height, the uncertainty of determining M' is a potential cause for creating different tropical precipitation anomalies among climate models. A constant M_s, which is also uniform in space, is usually used in a simplified climate model to avoid the uncertainty in determining convection height, such as in QTCM (CN04). The convection height is higher in deep convection regions, so M_s is larger. Thus, the constant M_s tends to reduce M and slightly overemphasize the dynamic feedback via $\nabla\cdot\mathbf{v}_1'$ in deep convection regions, vice versa for shallower convective regions. When a constant M_s is used, that is, $-\langle\overline{\omega}\,\partial_p s'\rangle = 0$, the term of $-\langle\overline{\omega}\,\partial_p q'\rangle$ becomes the main source for inducing the M' mechanism, such as in CN04.

The term $-\langle\overline{\mathbf{v}}\cdot\nabla q'\rangle$ is associated with the upped-ante mechanism if q' is associated with upper-level temperature anomalies in convective regions. A warm troposphere enhances low-level moisture in convective regions because of QE mediation, but not in nonconvective regions. This induces horizontal gradient of low-level moisture anomalies. The anomalous moisture gradient induces horizontal transport of dry air via the mean flow and suppresses convection over the margins of convective regions wherever there is inflow from nonconvective regions. The term $-\langle\overline{\mathbf{v}}\cdot\nabla T'\rangle$ is relatively small compared to $-\langle\overline{\mathbf{v}}\cdot\nabla q'\rangle$ in the Tropics, so the effect of $-\langle\overline{\mathbf{v}}\cdot\nabla T'\rangle$ is usually neglected, such as in CN04. However, QE mediation implies an increase in low-level moist static energy, and there can be a temperature contribution to this in addition to that of moisture.

The other terms of horizontal advection, $-\langle\mathbf{v}'\cdot\nabla\overline{T}\rangle$ and $-\langle\mathbf{v}'\cdot\nabla\overline{q}\rangle$, are dynamical feedbacks associated with $\mathbf{v}'$. This horizontal transport of moist static energy also induces regional precipitation anomalies and is similar to that occurring in El Niño in Pacific decent regions (Su and Neelin 2002). This effect has been defined as anomaly wind mechanisms by Neelin and Su (2005).

The surface net heat flux anomalies F_s' are balanced by ocean heat storage and heat transport. Ocean heat storage and transport can be roughly estimated from the spatial pattern of F_s' without knowing the ocean circulation. Ocean heat storage tends to have wider spatial patterns, while ocean heat transport divergence can create more local features. The net heat flux anomalies at TOA F_t' are associated with OLR and net solar radiation at TOA. Both longwave and solar radiation are strongly related to clouds, particularly in a regional scale, so F_t' can be treated as a cloud–radiative feedback. A part of F_t' that is associated with deep convection acts like modification of gross moist stability (Su and Neelin 2002). For instance, the TOA solar radiation associated with deep convection dominates F_t' in the QTCM simulations (Su and Neelin 2002). Thus,

$$F_t' \approx -a\nabla\cdot\mathbf{v}_1' < 0, \tag{10}$$

where a is a positive value. Replacing F_t' in (3) with (10) modifies the factor $\overline{M}$ with the addition of a. In other words, the shortwave cooling in regions of anomalous rising motion acts like a modification of $\partial_p\overline{h}$ in $\langle\omega'\partial_p\overline{h}\rangle$. In the Tropics, however, a near cancellation between the net TOA solar radiation and OLR is found over regions dominated by deep convection (Kiehl 1994; Cess et al. 2001; Hartmann et al. 2001).

A large-scale average of F_t' has very different balances than the regional variations discussed above. The average of the term on the left of (3) and the first four terms on the right is either close to zero over the global region or exhibits a very small exchange with midlatitudes if averaged over the Tropics. Then, balances among large-scale aspects of

$$[F_s'] + [F_t'] = 0, \tag{11}$$

where [] is spatial average, are crucial. These set the large-scale T' pattern through variations of longwave radiation and one can trace mechanisms for T' to regional tropical precipitation anomalies that are initiated by QE mediation.

Finally, we note that there are substantial technical challenges to computation of MSE budgets from standard GCM diagnostics. For instance, it has been known for some time that the sum of $\langle \omega \partial_p s \rangle$ and $\langle \omega \partial_p q \rangle$ terms has such a strong cancellation between large terms that estimation of the former from data interpolated to pressure levels can yield substantial error in the sum, and that contributions of transient terms can be nonnegligible (Neelin 1987). Overcoming these issues, as well as theoretical challenges in how to interpret cases where the conditions used in this section must be relaxed, is the subject of ongoing work. Here, working with standard diagnostics from an existing run, we side step these problems by focusing on key individual terms that are identified with particular mechanisms.

c. Diagnosis

In the study of CN04, QE mediation initiates a process that leads to anomalous precipitation under global warming. When the troposphere warms, low-level moisture tends to increase to maintain convective quasi equilibrium in convective regions. However, QE mediation does not occur in nonconvective regions where moisture is controlled by different processes, such as a balance between low-level divergence and evaporation that induce smaller increases in low-level moisture. The different processes controlling low-level moisture in convective and nonconvective regions create horizontal gradients of moisture anomalies. Thus, we first examine the distribution of low-level moisture in the GHG experiment. Then, $-(\mathbf{v} \cdot \nabla q)'$ and $-(\mathbf{v} \cdot \nabla T)'$ in the lower troposphere will be examined for the upped-ante mechanism. Finally, the term $-\langle \overline{\omega} \partial_p q' \rangle$ associated with the rich-get-richer mechanism and the $- \langle \omega' \partial_p \overline{q} \rangle$ feedbacks should also be examined in the ECHAM4/OPYC3 simulations.

Figure 8 shows anomalous moisture in the ABL (1000–900 hPa) and a free atmospheric layer just above the ABL (900–700 hPa). The results indicate that moisture over the convective regions is enhanced not only in the ABL, but also in the free troposphere. The moisture increases are comparable in magnitude between the ABL and the 900–700-hPa layer with both having maximum values in deep convection regions. Moisture in the ABL increases due to surface warming even over nonconvective regions, but the ABL moisture increases are larger in convective regions (the thick solid line in Fig. 8.), enhanced by QE mediation. Convection can further transport moisture into the free atmosphere. Moisture anomalies the 900–700-hPa layer thus have very sharp maxima in convective regions. These moisture anomalies create horizontal gradients of anomalous moisture from convective regions to nonconvective regions. Besides the maximum moisture anomalies in convective regions, local maxima of the low-level moisture anomalies are also found over the central and eastern Pacific where the positive precipitation anomalies also have a maximum. Another set of local maxima of low-level moisture anomalies is found in the boreal summer over the northern margin of the convective region from Africa, across the Arabian Peninsula, to the northern Indian Peninsula. Note that the Asia summer regions also have a local maximum of low-level moisture anomalies. Thus, the maximum moisture

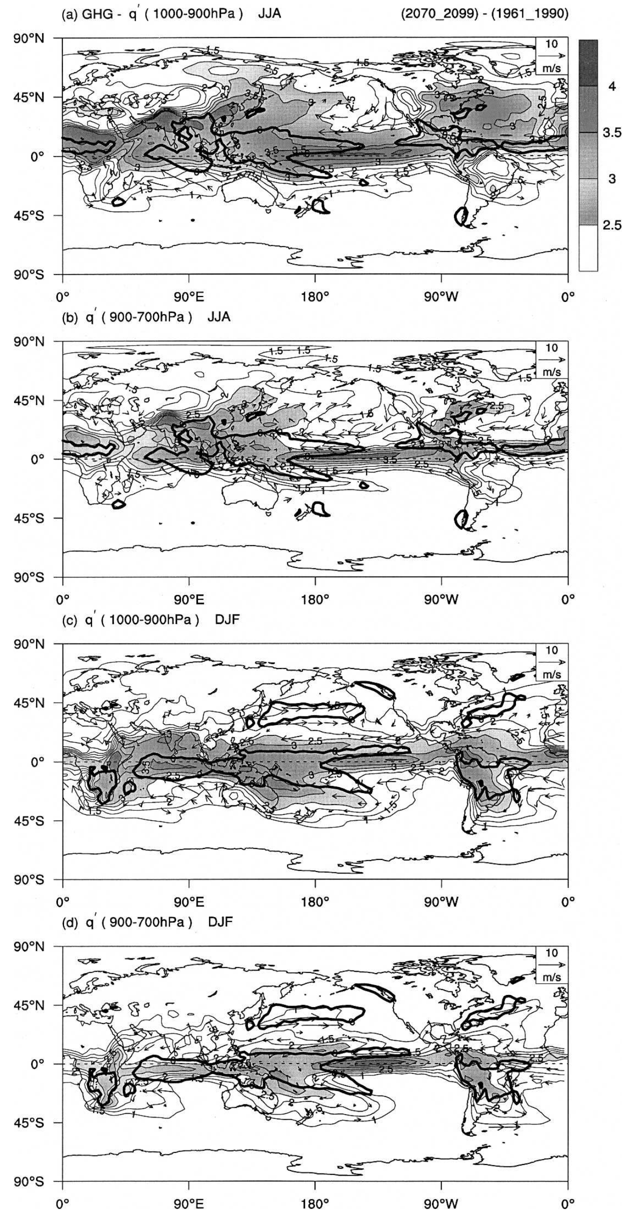

FIG. 8. Same as in Fig. 4 except for moisture anomalies (g kg^{-1} in the 1000–900-hPa layer in (a) JJA and (c) DJF and the 900–700-hPa layer in (b) JJA and (d) DJF. Climatological winds in 1961–90 near margins of convective regions are also plotted for the same layer averages. The thick solid line is the 6 mm day^{-1} contour of the precipitation climatology in 1961–90.

anomalies are consistently found over the northern edge of the summer monsoon rainband starting from Africa to East Asia.

Considering the horizontal gradient of the moisture anomalies, the next step is to examine horizontal advection of moisture in the anomaly field, which may be associated with the upped-ante mechanism discussed by CN04. In the Tropics, the term of $-\mathbf{v}' \cdot \nabla \overline{q}$ is generally smaller than the term of $-\overline{\mathbf{v}} \cdot \nabla q'$. The only exception is the band of increased moisture in JJA in Africa and East Asia noted above, which is associated with $-\mathbf{v}' \cdot \nabla \overline{q}$ (not shown). Elsewhere, the distribution of $-\overline{\mathbf{v}} \cdot \nabla q'$ is similar to the distribution of $-(\mathbf{v} \cdot \nabla q)'$ shown in Fig. 9. The mean winds in the lower troposphere are plotted over margins of convective regions for climatological moisture between 3 and 10 g kg^{-1} to indicate the regions with possible inflow of dry air (Fig. 8). In JJA, strong inflow of dry air is found over the southern Indian Ocean, the eastern end of SPCZ, and the northern edge of South America. In DJF, strong inflow of dry air is also found on the north and south sides of the Indian Ocean convective region, the eastern end of SPCZ, the eastern part of South America and Africa. All these areas are consistent with negative moisture transport anomalies found in Fig. 9. Overall, the largest horizontal moisture transport anomalies $-(\mathbf{v} \cdot \nabla q)'$ shown in Fig. 9 can be seen by examining the mean flow in Fig. 8, although the pattern of $-(\mathbf{v} \cdot \nabla q)'$ also contains complex details. The magnitude of the horizontal moisture transport in the 700–900-hPa layer is as strong as in the ABL, so the transport in the lower free troposphere also plays an important role in the upped-ante mechanism. This was also true in CN04, but that study could not distinguish between the ABL and lower free-tropospheric transports.

In nonconvective regions, $-(\mathbf{v} \cdot \nabla q)'$ has no impact on precipitation. In convective regions, on the other hand, most negative anomalous moisture transport coincides with negative precipitation anomalies shown in Figs. 4a,b (also the thick dashed line in Fig. 9). This supports the hypothesis that the negative precipitation anomalies are induced by the upped-ante mechanism over these regions. Note that the effect of $-\overline{\mathbf{v}} \cdot \nabla q'$ can also directly contribute the anomalous precipitation in (2). More importantly, $-\overline{\mathbf{v}} \cdot \nabla q'$ can affect regional precipitation via the dynamical feedback that is associated with effects on ω' via the MSE balance, which can be stronger than its direct effect. To further examine the upped-ante mechanism, the South American region in DJF is chosen as an example since this region has also been discussed as a target region dominated by the upped-ante mechanism in CN04. Dry advection of moisture anomalies is found over northeast Brazil, with

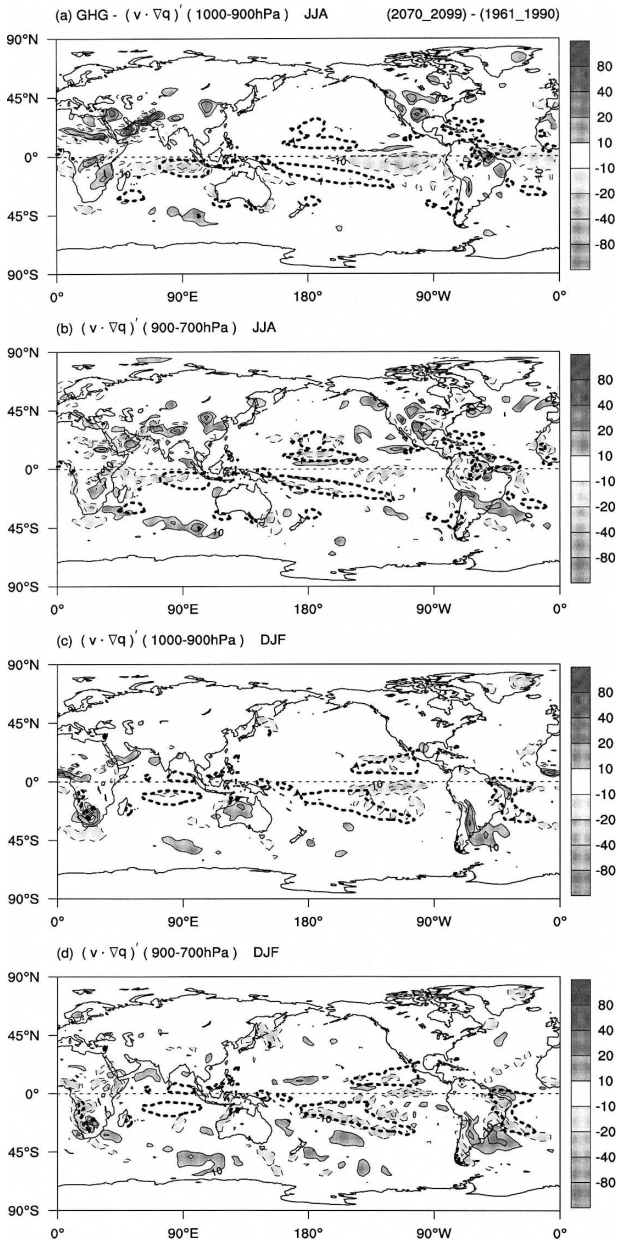

FIG. 9. Same as in Fig. 8 except for $-(\mathbf{v} \cdot \nabla q)'$ (W m^{-2}). The thick dashed line is the -1 mm day^{-1} contour of the precipitation anomalies obtained from Fig. 4.

the dry advection in the free atmosphere contributing more than the ABL dry advection. This indicates that the moisture transport in the lower free troposphere is more important than ABL moisture transport over South America. Other regions, such as the southern Pacific and southwestern Africa, are also dominated by lower free-troposphere dry advection. One exception is found over the northeastern tip of South America and the neighboring Atlantic Ocean, which show positive anomalous moisture transport (Figs. 9b,d), but negative precipitation anomalies (Fig. 4b). Over this region, negative surface heat flux anomalies (Fig. 7d) offset the moist advection and induce the negative precipitation anomalies. Thus, an ocean dynamical feedback induces the negative precipitation anomalies over a small part of the Atlantic Ocean just north of Brazil, while the upped-ante mechanism contributes the rest of the negative precipitation anomalies over the South America–Atlantic region.

The other term that also has a similar contribution to the upped-ante mechanism is $-\overline{\mathbf{v}} \cdot \nabla T'$ when transporting cold air from outside convective regions. The term $-\mathbf{v}' \cdot \nabla \overline{T}$ is relatively small compared to $-\overline{\mathbf{v}} \cdot \nabla T'$, so $-\overline{\mathbf{v}} \cdot \nabla T'$ can be used to represent the effect of $-(\mathbf{v} \cdot \nabla T)'$ shown in Fig. 10. Over tropical oceans, $-(\mathbf{v} \cdot \nabla T)'$ is very small. Over tropical continents, some negative $-(\mathbf{v} \cdot \nabla T)'$ is found over Brazil, the southwestern coast of Africa, and the western coast of Australia (Fig. 10). Over the southwestern coast of Africa and the western coast of Australia, negative $-(\mathbf{v} \cdot \nabla T)'$ is consistent with negative $-(\mathbf{v} \cdot \nabla q)'$, so the upped-ante mechanism has been enhanced. However, negative $-(\mathbf{v} \cdot \nabla T)'$ contributes in a narrow band between the region of strong negative $-(\mathbf{v} \cdot \nabla q)'$ over Brazil and the equatorial Atlantic just north of Brazil in DJF where negative F_s' contributes to negative precipitation anomalies. This again indicates somewhat more complicated processes inducing negative precipitation anomalies over the South America–Atlantic region in DJF than that indicated by CN04. To look at the changes over the South American region in DJF more closely, the precipitation increases about 0.29 mm day^{-1} over the convective region, while it decreases about -0.59 mm day^{-1} over the margins of convective region (3 mm day$^{-1} \leq \overline{P} \leq 6$ mm day^{-1}; Fig. 11a). The negative precipitation anomalies coincide with negative $-[\mathbf{v} \cdot \nabla(T + q)]'$ in the 1000–700-hPa layer (Fig. 11b), evidence of the upped-ante mechanism. However, the upped-ante mechanism is not only from the contribution of $-(\mathbf{v} \cdot \nabla q)'$ (Fig. 11c), but also $-(\mathbf{v} \cdot \nabla T)'$, especially over Brazil (Fig. 11d).

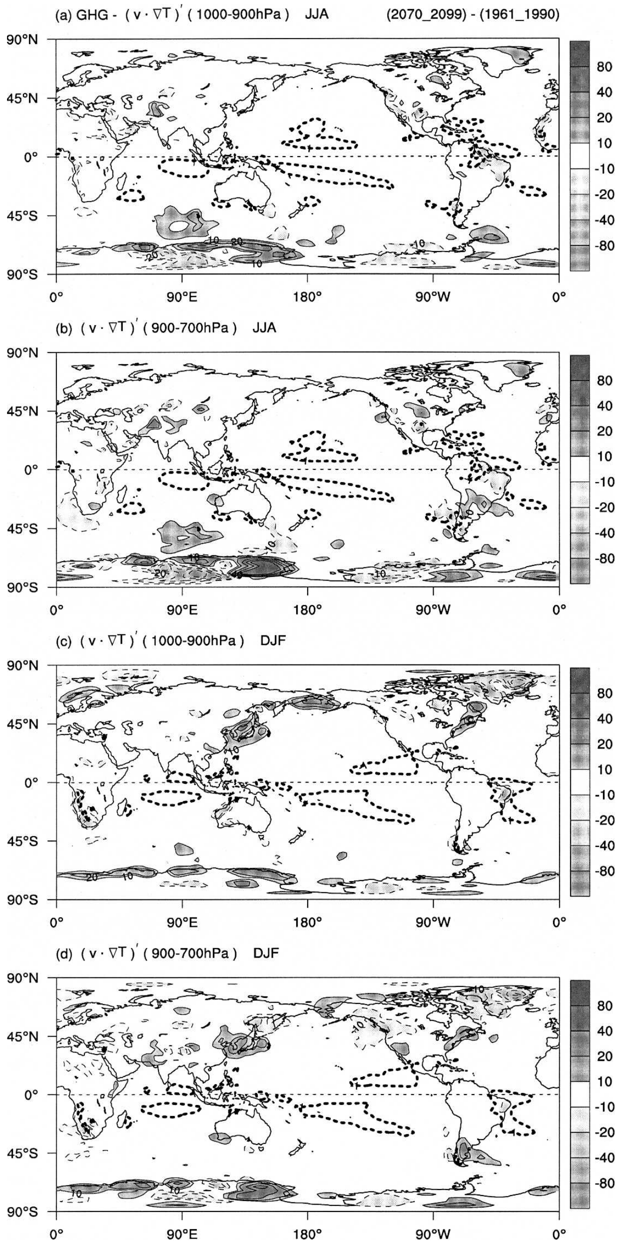

FIG. 10. Same as in Fig. 8 except for $-(\mathbf{v} \cdot \nabla T)'$ (W m^{-2}).

Computation of $\langle \omega \partial_p h \rangle'$, involves challenges discussed at the end of section 5b, affecting the use of $\langle \omega \partial_p s \rangle'$. We thus neglect the contribution of $\langle \omega \partial_p s \rangle'$ and focus on the effect of $\langle \omega \partial_p q \rangle'$ in this study. Neglecting the term $\langle \omega \partial_p s \rangle'$ will not close the MSE budget, but mechanisms associated with $\langle \omega \partial_p q \rangle'$ and other terms that induce anomalous vertical motion (ω') can still be discussed. Figure 12 shows the distributions of $-\langle \omega' \partial_p \overline{q} \rangle$ and $-\langle \overline{\omega} \partial_p q' \rangle$. The term $-\langle \omega' \partial_p \overline{q} \rangle$ can be used to roughly represent lower-tropospheric convergence since moisture is concentrated in the lower troposphere. The term $-\langle \omega' \partial_p \overline{q} \rangle$ in Figs. 12b,d is very similar to the precipitation anomalies shown in Figs. 4a,b. According to the moisture budget equation (2), $-\langle \omega' \partial_p \overline{q} \rangle$ contributes more than 80% of the anomalous precipitation in the Tropics. Other effects, such as $-\langle \overline{\omega} \partial_p q' \rangle$, $-\overline{\mathbf{v}} \cdot \nabla q'$ and E', contribute a combined 20% of the anomalous precipitation. Thus, the dynamical feedback associated with ω' is the most important effect for inducing the anomalous precipitation (consistent with NCS03 and CN04).

The term $-\langle \overline{\omega} \partial_p q' \rangle$ can directly contribute to anoma-

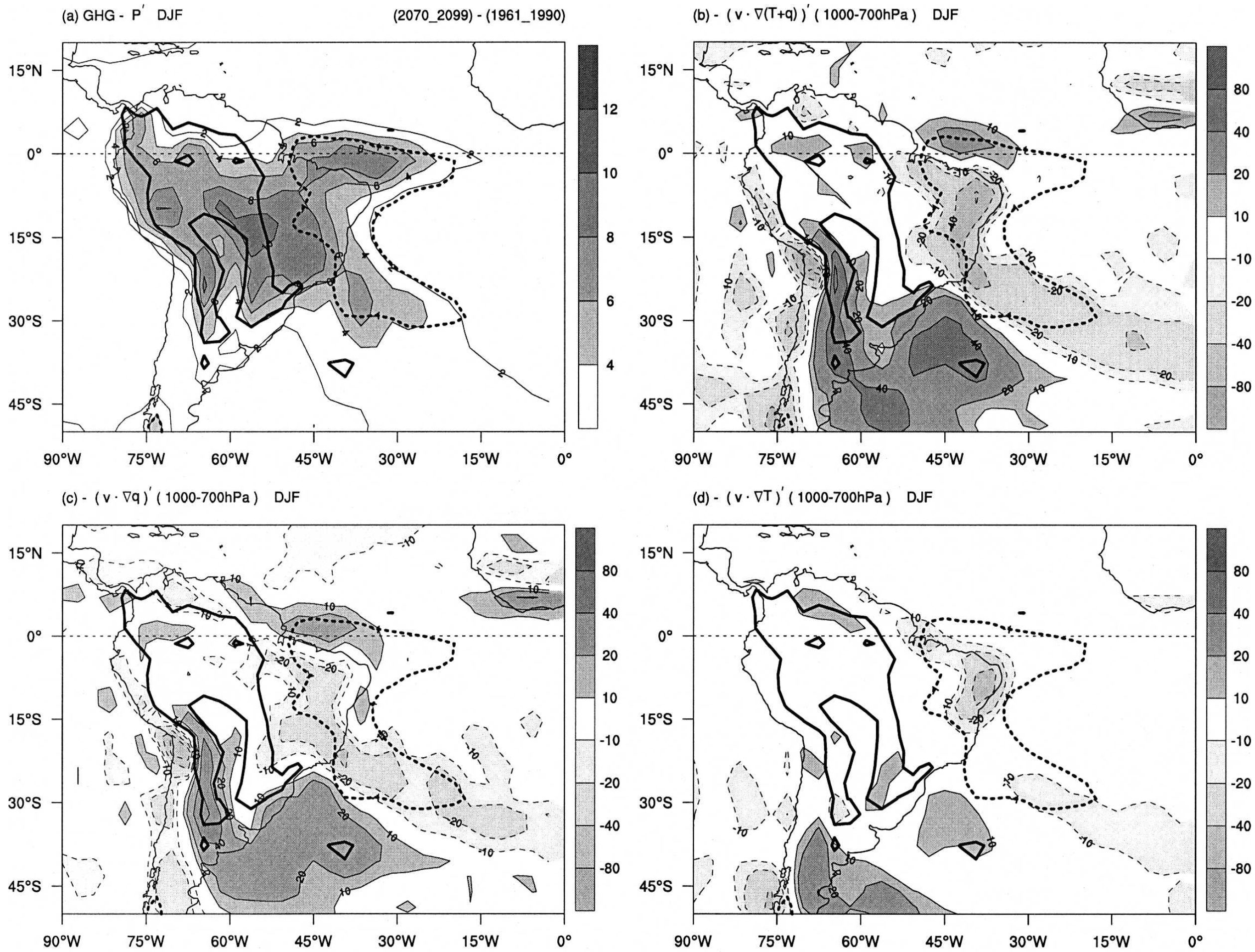

FIG. 11. Differences for the GHG experiment 2070–99 minus 1961–90 averages in DJF: (a) precipitation climatology, (b) $-\langle \mathbf{v} \cdot \nabla(T + q)\rangle'$ (W m^{-2}) in the 1000–700-hPa layer, (c) $-\langle \mathbf{v} \cdot \nabla q\rangle'$ in the 1000–700-hPa layer, and (d) $-\langle \mathbf{v} \cdot \nabla T\rangle'$ in the 1000–700-hPa layer. The thick solid and dashed lines are ± 1 mm day^{-1} contours of the precipitation anomalies obtained from Fig. 4.

lous precipitation in the moisture budget (2), but it can also affect the anomalous precipitation via the dynamical feedback in (3). In CN04, this term is equivalent to the M' mechanism because of the assumption of $-\langle \overline{\omega} \partial_p s' \rangle = 0$. Figures 12a,c show the pattern of $-\langle \overline{\omega} \partial_p q' \rangle$ which is similar to that of mean convection. In other words, the M' mechanism associated with low-level moisture enhances convection over deep convection regions, consistent with CN04. In convective regions, the contribution of $-\langle \overline{\omega} \partial_p q' \rangle$ is a dominant effect inducing positive precipitation anomalies compared to the other effects shown on the rhs. of (9) and it contributes 80% or more of the positive precipitation anomalies over convective regions.

Another effect on regional precipitation is associated with the net energy into the atmospheric column F^{net}, which can be divided into F_t and F_s. The term F_s', due to ocean heat storage and transport has been discussed in section 4. On the other hand, F_t' is associated mainly with the cloud–radiative feedback in the Tropics because longwave and solar radiation anomalies depend strongly on convective clouds. Figure 13 shows the distribution of F_t' in JJA and DJF. Over tropical oceans, negative F_t' coincides with positive precipitation anomalies, and vice versa for positive F_t'. This implies that solar radiative cooling effect is larger than the longwave radiative warming effect, so net negative cloud–radiative feedback is found over tropical oceans. Since the convective clouds are closely correlated with vertical motion, the F_t' cooling effect acts like a modification of $\partial_p \overline{h}$ in (3). Over some land regions, such as the central Amazon, F_t' exhibits a different and complicated relation with the regional precipitation. Positive precipitation anomalies are associated with positive F_t', implying a positive cloud–radiative feedback over this region. This might result from different cloud types. For

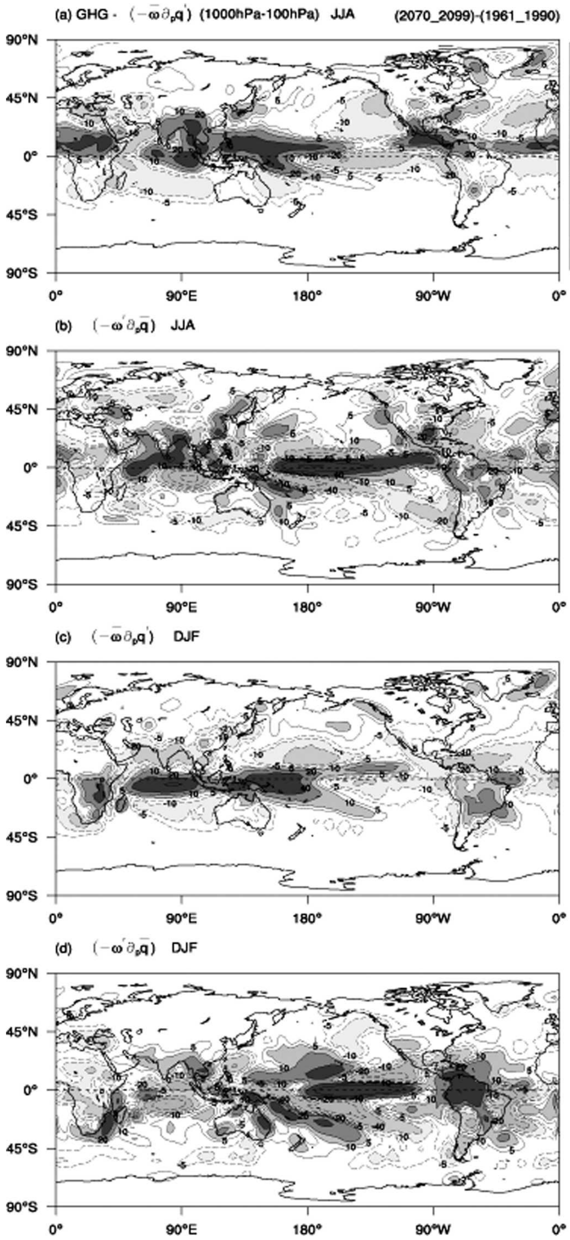

FIG. 12. Same as in Fig. 8 except for $-\langle\overline{\omega}\partial_p q'\rangle$ in (a) JJA and (c) DJF and $-\langle\omega'\partial_p\overline{q}\rangle$ in (b) JJA and (d) DJF. The vertical average is from 1000 to 100 hPa Units: W m^{-2}.

instance, more thin cirrus clouds can enhance longwave radiative warming without much solar radiative cooling, producing positive F_t'. Another possible reason for this positive cloud–radiative feedback is associated with larger surface albedo over land (Neelin and Su 2005). Larger surface albedo weakens the shortwave cloud–radiative feedback, but not the longwave feedback, so the net cloud–radiative feedback can become positive. The global average of F_t' is slightly positive. This indicates that the warming due to the greenhouse effect is

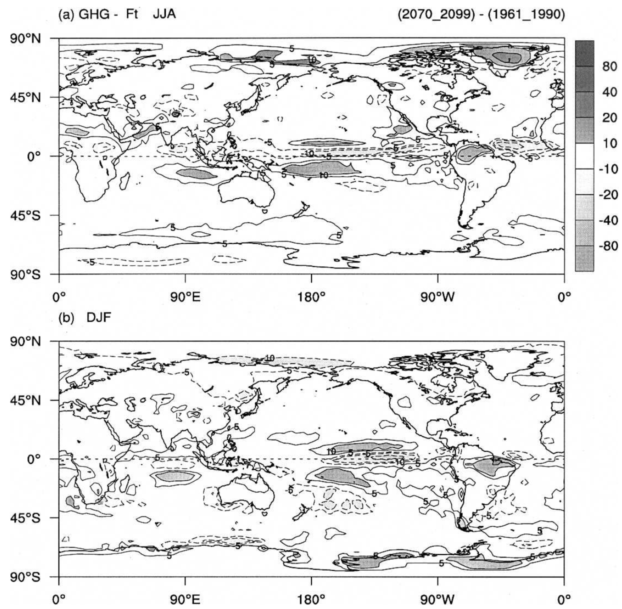

FIG. 13. Same as in Fig. 8 except for F'_t (W m^{-2}) in (a) JJA and (b) DJF.

not in equilibrium. Combined with the negative F_s' discussed before, the global average of $F^{\mathrm{net}\prime}$ is close to zero.

6. Summary and discussion

Impacts of global warming on regional tropical precipitation involve complex processes that are not well understood. Analyzing ECHAM4 AOGCM simulations with theory derived from an atmospheric model of intermediate complexity coupled with a mixed layer ocean (CN04), we examine mechanisms of global warming impacts on regional tropical precipitation.

The anthropogenic forcings include the effects of greenhouse gases and sulfate aerosol. In these ECHAM4 AOGCM simulations, the GHG contribution is the leading effect in regional tropical precipitation changes by 2021–50. Aerosol impacts tend to reduce the GHG signal in early periods. The pattern of the tropical precipitation anomalies induced by the greenhouse effect tends to persist and grow over the century. In other words, the pattern of the regional precipitation anomalies in the latter stage, such as 2070–99, has already been established in the earlier stage (2021–50 is shown here), and the main change is the amplitude of the precipitation anomalies. Comparing runs with and without sulfate aerosol, overall, the aerosol effect reduces the regional precipitation anomalies in magnitude and cools the whole troposphere. The effect on the tropical precipitation via the tropospheric temperature anomalies has been termed the aerosol remote effect in

Chou et al. (2005). Aerosol local impacts on tropical precipitation change appear to be secondary in these experiments.

The ocean affects the atmosphere via net surface flux anomalies F_s', which are balanced by ocean heat storage and transport. Under global warming, ocean heat storage creates widespread negative F_s'. The atmosphere is losing energy into the ocean, so atmospheric warming is delayed by ocean heat storage (Manabe et al. 1991). Effects on tropical precipitation mediated by tropospheric temperature changes are correspondingly delayed, an effect that may be important in the early period of the global warming. A separate effect occurs through ocean dynamical feedback via ocean circulation changes and the associated ocean heat transport. Unlike the ocean heat storage, the ocean heat transport produces large F_s' locally, which affects regional tropical precipitation via effects on the energy budget and the associated vertical motion. In the ECHAM4 AOGCM global warming simulations, positive F_s' is found over the eastern Pacific, associated with an El Niño–like SST anomaly pattern. The positive F_s' enhances local upward motion and convection over the eastern Pacific through the MSE balance in (3). Thus, strong positive precipitation anomalies are found over the eastern Pacific. Besides the local impacts of the El Niño–like F_s', El Niño–like teleconnections can also affect regional precipitation. The negative precipitation anomalies in the eastern Pacific are similar to the well-known horseshoe pattern of subsidence during El Niño events.

The net heat flux at TOA F_t' represents a cloud–radiative feedback in convective regions and plays a role in the magnitude of regional tropical precipitation anomalies. Over the tropical ocean, shortwave cloud–radiative cooling dominates and longwave cloud–radiative warming is relatively weak, so the net cloud–radiative feedback is negative, acting to reduce regional tropical precipitation anomalies. Over some tropical continental regions, however, the cloud–radiative feedback associated with F_t' is more complicated, possibly due to different cloud types and land surface albedo.

Under global warming, two main mechanisms associated with atmospheric dynamical feedbacks via ω', which have been discussed in CN04 are examined here: the upped-ante mechanism and the M' mechanisms. The upped-ante mechanism is one possible source for tropical drought in global warming simulations and this mechanism has been proposed in NCS03 and CN04 with an intermediate atmospheric model coupled with a mixed layer ocean. In this study, we find evidence for the upped-ante mechanism in the ECHAM4 simulations, although with slight modification. To initiate the upped-ante mechanism, horizontal gradients of low-level moisture anomalies induced by QE mediation should occur. In the ECHAM4 simulations, stronger positive moisture anomalies are found in convective regions, while weaker positive moisture anomalies are found in nonconvective regions. For those regions where the mean flow is from nonconvective regions to convective regions, evidence of the import of dry air is found. The regions with the dry air import coincide with negative tropical precipitation anomalies. This suggests that the dry air import associated with the upped-ante mechanism is responsible for the regional precipitation reductions. While NCS03 and CN04 emphasized the ABL, here we find the dry air import occurs not only in the ABL, but also in the lower free-tropospheric layer. In some places, eastern South America for instance, the drying advective tendency in the lower free troposphere is even stronger than that in the ABL. The importance of the moisture transport in the lower free troposphere (700–900 hPa) implies that the vertical moisture transport by convection is important to the horizontal moisture gradient in the upped-ante mechanism. Besides the dry air import, the energy transport associated with the ABL temperature gradient can also have a similar contribution to the upped-ante mechanism since the colder ABL has lower moist static energy, which disfavors convection. Overall, the upped-ante mechanism associated with horizontal moisture transport is one major effect, although not the only one, inducing negative precipitation anomalies in the Tropics. Other effects, such as $-(\mathbf{v} \cdot \nabla T)'$ and F_s' can also play a role in inducing negative precipitation anomalies.

Another important mechanism for inducing positive regional tropical precipitation anomalies is the M' mechanism. The gross moist stability M depends on low-level moisture and depth of convection. The low-level moisture effect is associated with the term $-\langle\overline{\omega}\partial_p q'\rangle$, which is equivalent to $-M_q'\nabla \cdot \overline{\mathbf{v}}_1$ in CN04, while the effect of the depth of convection is associated with $-\langle\overline{\omega}\partial_p s'\rangle$ (or $-M_s'\nabla \cdot \overline{\mathbf{v}}_1$). The M' mechanism discussed in CN04 is associated with the low-level moisture change. The increased low-level moisture reduces the stability of the atmosphere in convective regions and this enhances convection in strong convection regions. In the ECHAM4 results here, the tropical precipitation anomalies do increase over most strong convective regions, except over the western Pacific warm pool, which might be controlled by the El Niño–like teleconnection. Our budget analysis here is subject to the caveat that we have not been able to assess possible compensating effects by the depth of convection. However, we find that positive $-\langle\overline{\omega}\partial_p q'\rangle$ over convective regions has a clear association with positive precipitation anomalies, thus providing evidence for the impact of the M' or the rich-get-richer mechanism in ECHAM4.

When assessing other GCM results for signatures of the upped-ante and M' mechanisms, the following is a list of things that can be examined:

1) increased moisture in the ABL and lower free troposphere in convection zones;
2) association of advecting drying tendency $-\langle \mathbf{v} \cdot \nabla q \rangle'$ with negative precipitation anomalies in margins of convective regions;
3) association of positive $-\langle \overline{\omega} \partial_p q' \rangle$ with positive precipitation anomalies within convection zones; and
4) $-\langle \omega' \partial_p \overline{q} \rangle$ feedbacks enhancing the signals of items 2 and 3 above.

Acknowledgments. We thank the Global Climate Modeling group at the Max Planck Institute for Meteorology, Hamburg, Germany, especially Dr. E. Roeckner and Ms. Monika Esch, for providing access to data from their simulations. The corresponding author particularly thanks Dr. Jia-Yuh Yu for useful comments. This work was supported under National Science Council Grant 93-2111-M-001-001, the National Science Foundation Grant ATM-0082529, and the National Oceanic and Atmospheric Administration Grant NA05OAR431134.

REFERENCES

Allen, M. R., and W. J. Ingram, 2002: Constraints on future changes in climate and the hydrologic cycle. *Nature,* **419,** 224–232.

Boer, G. J., G. Flato, and D. Ramsden, 2000: A transient climate change simulation with green-house gas and aerosol forcing: Projected climate to the twenty-first century. *Climate Dyn.,* **16,** 427–450.

Cess, R. D., M. Zhang, B. A. Wielicki, D. F. Young, X. L. Zhou, and Y. Nikitenko, 2001: The influence of the 1998 El Niño upon cloud-radiative forcing over the Pacific warm pool. *J. Climate,* **14,** 2129–2137.

Chou, C., and J. D. Neelin, 2004: Mechanisms of global warming impacts on regional tropical precipitation. *J. Climate,* **17,** 2688–2701.

——, ——, U. Lohmann, and J. Feichter, 2005: Local and remote impacts of aerosol climate forcing on tropical precipitation. *J. Climate,* **18,** 4621–4636.

Dai, A., G. A. Meehl, W. M. Washington, T. M. L. Wigley, and J. M. Arblaster, 2001a: Ensemble simulation of twenty-first century climate changes: Business-as-usual versus CO_2 stabilization. *Bull. Amer. Meteor. Soc.,* **82,** 2377–2388.

——, T. M. L. Wigley, B. A. Boville, J. T. Kiehl, and L. E. Buja, 2001b: Climates of the twentieth and twenty-first centuries simulated by the NCAR climate system model. *J. Climate,* **14,** 485–519.

Delworth, T. L., and T. R. Knutson, 2000: Simulation of early 20th century global warming. *Science,* **287,** 2246–2250.

Douville, H., F. Chauvin, S. Planton, J.-F. Royer, D. Salas-Mélia, and S. Tyteca, 2002: Sensitivity of the hydrological cycle to increasing amounts of greenhouse gases and aerosol. *Climate Dyn.,* **20,** 45–68.

Hansen, J., M. Sato, and B. Ruedy, 1995: Long-term changes of the diurnal temperature cycle—Implications about mechanisms of global climate-change. *Atmos. Res.,* **37,** 175–209.

Hartmann, D. L., L. A. Moy, and Q. Fu, 2001: Tropical convection and the energy balance at the top of the atmosphere. *J. Climate,* **14,** 4495–4511.

Held, I. M., and B. J. Soden, 2000: Water vapor feedback and global warming. *Annu. Rev. Energy Environ.,* **25,** 441–475.

Houghton, J. T., B. A. Callander, and S. K. Varney, Eds., 1992: *The Supplementary Report to the IPCC Scientific Assessment.* Cambridge University Press, 198 pp.

——, Y. Ding, D. J. Griggs, M. Noguer, P. J. van der Linden, X. Dai, K. Maskell, and C. A. Johnson, Eds., 2001: *Climate Change 2001: The Scientific Basis.* Cambridge University Press, 881 pp.

Jin, F.-F., Z.-Z. Hu, M. Latif, L. Bengtsson, and E. Roeckner, 2001: Dynamical and cloud-radiation feedbacks in El Niño and greenhouse warming. *Geophys. Res. Lett.,* **28,** 1539–1542.

Kiehl, J. T., 1994: On the observed near cancellation between longwave and shortwave cloud forcing in tropical regions. *J. Climate,* **7,** 559–565.

Knutson, T. R., and S. Manabe, 1998: Model assessment of decadal variability and trends in the tropical Pacific Ocean. *J. Climate,* **11,** 2273–2296.

Lucarini, V., and G. L. Russell, 2002: Comparison of mean climate trends in the Northern Hemisphere between National Centers for Environmental Prediction and two atmosphere-ocean model forced runs. *J. Geophys. Res.,* **107,** 4269, doi:10.1029/2001JD001247.

Manabe, S., R. J. Stouffer, M. J. Spelman, and K. Bryan, 1991: Transient responses of a coupled ocean-atmosphere model to gradual changes of atmospheric CO_2. Part I: Annual mean response. *J. Climate,* **4,** 785–818.

Meehl, G. A., and W. M. Washington, 1996: El Niño-like climate change in a model with increased atmospheric CO_2 concentrations. *Nature,* **382,** 56–60.

——, W. D. Collins, B. A. Boville, J. T. Kiehl, T. M. L. Wigley, and J. M. Arblaster, 2000: Response of the NCAR climate system model to increased CO_2 and the role of physical processes. *J. Climate,* **13,** 1879–1898.

——, W. M. Washington, T. M. L. Wigley, J. M. Arblaster, and A. Dai, 2003: Solar and greenhouse gas forcing and climate response in the twentieth century. *J. Climate,* **16,** 426–444.

——, ——, W. D. Collins, J. M. Arblaster, A. Hu, L. E. Buja, W. G. Strand, and H. Teng, 2005: How much more global warming and sea level rise? *Science,* **307,** 1769–1772.

Mitchell, J. F. B., W. J. Ingram, and J. A. Lowe, 2000: The effect of stabilizing atmospheric carbon dioxide concentration on global and regional climate change. *Geophys. Res. Lett.,* **27,** 2977–2980.

Neelin, J. D., 1987: Simple models of steady and low-frequency circulations in the tropical atmosphere, with application to tropical air-sea interactions. Ph.D. dissertation, Princeton University, 240 pp.

——, and N. Zeng, 2000: A quasi-equilibrium tropical circulation model—Formulation. *J. Atmos. Sci.,* **57,** 1741–1766.

——, and H. Su, 2005: Moist teleconnection mechanisms for the tropical South American and Atlantic sector. *J. Climate,* **18,** 3928–3950.

——, C. Chou, and H. Su, 2003: Tropical drought regions in global warming and El Niño teleconnections. *Geophys. Res. Lett.,* **30,** 2275, doi:10.1029/2003GL018625.

Noda, A., K. Yamaguchi, S. Yamaki, and S. Yukimoto, 1999: Relationship between natural variability and CO_2-induced warming pattern: MRI AOGCM experiment. Preprints, *10th Symp. on Global Change Studies,* Dallas, TX, Amer. Meteor. Soc., 359–362.

Oberhuber, J. M., 1993: The OPYC ocean general circulation model. DKRZ Rep. 7, Deutsches Klimarechenzentrum, Hamburg, Germany, 130 pp.

Roeckner, E., and Coauthors, 1996: The atmospheric general circulation model ECHAM-4: Model description and simulation of present-day climate. Max-Planck-Institut für Meteorologie, Rep. 218, 90 pp.

——, L. Bengtsson, J. Feichter, J. Lelieveld, and H. Rodhe, 1999: Transient climate change simulation with a coupled atmosphere-ocean GCM including the tropospheric sulfur cycle. *J. Climate,* **12,** 3004–3032.

Su, H., and J. D. Neelin, 2002: Teleconnection mechanisms for tropical Pacific descent anomalies during El Niño. *J. Atmos. Sci.,* **59,** 2694–2712.

——, ——, and J. E. Meyerson, 2003: Sensitivity of tropical tropospheric temperature to sea surface temperature forcing. *J. Climate,* **16,** 1283–1301.

Tett, S. F. B., 1995: Simulation of El Niño–Southern Oscillation-like variability in a global coupled AOGCM adn its response to CO_2 increase. *J. Climate,* **8,** 1473–1502.

Wallace, J. M., T. P. Mitchell, E. M. Rasmusson, V. E. Kousky, E. S. Sarachik, and H. von Storch, 1998: On the structure and evolution of ENSO-related climate variability in the tropical Pacific: Lessons. *J. Geophys. Res.,* **103,** 14 241–14 259.

Washington, W. M., and Coauthors, 2000: Parallel climate model (PCM) control and transient simulations. *Climate Dyn.,* **16,** 755–774.

Watterson, I. G., 2003: Effects of a dynamic ocean on simulated climate sensitivity to greenhouse gases. *Climate Dyn.,* **21,** 197–209.

——, and M. R. Dix, 1999: A comparison of present and doubled CO_2 climates and feedbacks simulated by three general circulation models. *J. Geophys. Res.,* **104,** 1943–1956.

——, S. P. O'Farrell, and M. R. Dix, 1997: Energy and water transport in climates simulated by a general circulation model that includes dynamic sea ice. *J. Geophys. Res.,* **102,** 1943–1956.

Williams, K. D., C. A. Senior, and J. F. B. Mitchell, 2001: Transient climate change in the Hadley Centre models: The role of physical processes. *J. Climate,* **14,** 2659–2674.

Yonetani, T., and H. B. Gordon, 2001: Simulated changes in the frequency of extremes and regional features of seasonal/annual temperature and precipitation when atmospheric CO_2 is doubled. *J. Climate,* **14,** 1765–1779.

Yu, J.-Y., C. Chou, and J. D. Neelin, 1998: Estimating the gross moist stability of the tropical atmosphere. *J. Atmos. Sci.,* **55,** 1354–1372.

Zeng, N., J. D. Neelin, and C. Chou, 2000: A quasi-equilibrium tropical circulation model-implementation and simulation. *J. Atmos. Sci.,* **57,** 1767–1796.